



Drainage basin delineation for outlet glaciers of Northeast Greenland based on Sentinel-1 ice velocities and TanDEM-X elevations

Lukas Krieger^{a,*}, Dana Floricioiu^a, Niklas Neckel^b

^a Remote Sensing Technology Institute, German Aerospace Center (DLR), Oberpfaffenhofen, Germany

^b Alfred Wegener Institute for Polar and Marine Research, Bremerhaven, Germany

ARTICLE INFO

Keywords:

Drainage basin
Watershed
Glacier catchment
Monte-Carlo simulation
Ice sheet
Greenland

ABSTRACT

The drainage divides of ice sheets separate the overall glaciated area into multiple sectors. These drainage basins are essential for partitioning mass changes of the ice sheet, as they specify the area over which basin specific measurements are integrated. The delineation of drainage basins on ice sheets is challenging due to their gentle slopes accompanied by local terrain disturbances and complex patterns of ice movement. Until now, in Greenland the basins have been mostly delineated along the major ice divides, which results in large drainage sectors containing multiple outlet glaciers. However, when focusing on measuring glaciological parameters of individual outlet glaciers, more detailed drainage basin delineations are needed. Here we present for the first time a detailed and fully traceable approach that combines ice sheet wide velocity measurements by Sentinel-1 and the high resolution TanDEM-X global DEM to derive individual glacier drainage basins. We delineated catchments for the Northeast Greenland Ice Sheet with a modified watershed algorithm and present results for 31 drainage basins. Even though validation of drainage basins remains a difficult task, we estimated basin probabilities from Monte-Carlo experiments and applied the method to a variety of different ice velocity and DEM datasets finding discrepancies of up to 16% in the extent of catchment areas. The proposed approach has the potential to produce drainage areas for the entirety of the Greenland and Antarctic ice sheets.

1. Introduction

With the advance of remote sensing sensors, the mass balance estimates of Greenland and Antarctica are getting more and more accurate (Shepherd et al., 2012; Mouginit et al., 2019). Altimetry, gravimetry and SAR-based methods are now regularly used to monitor glaciers on a large scale for a whole ice sheet or for major drainage basins (Helm et al., 2014; Schröder et al., 2019; Sasgen et al., 2012; Groh et al., 2014; King et al., 2018; Mouginit et al., 2019). This is important to infer ice sheet wide physical processes and predict future sea level change. In these studies, glacier basins provide information about the geometric extent of the observed glacier systems and make the mass balance estimates comparable. In the present work, for the purpose of consistency, we use the terms drainage basin and glacier catchment interchangeably but always refer to the area of ice that is completely drained by a single outlet glacier. Multiple aggregated drainage basins form a drainage sector (e.g. the Northeast Greenland Ice Stream - NEGIS) whereas, on an even larger scale, the term drainage region refers to an aggregation of several drainage sectors (e.g. Northeast Greenland).

Until now the ice sheets' drainage sectors have been mostly separated along the major ice divides. Due to the gentle slopes for large parts of the ice sheets, they have only been processed at coarse resolutions, sometimes with additional modelled data (Hardy et al., 2000; Lewis and Smith, 2009). A widely used dataset for drainage sectors has been published by the NASA Goddard Space Flight Center (Zwally et al., 2012, Fig. 1). It utilises data from the ICESat Geoscience Laser Altimeter System (GLAS) and is available for both Greenland and Antarctica. Many ice sheet wide campaigns report mass balance estimates according to this delineation including the ESA/NASA ice sheet mass balance inter-comparison exercise (IMBIE) (Shepherd et al., 2012). The second assessment IMBIE-2 (Shepherd et al., 2018) included another published dataset of drainage sectors which was made available by Rignot and Mouginit (2012) and relies on an ERS/ICESat DEM in the interior of the ice sheets with additional velocity information near the coast. While these sources provide excellent basin information for mass balance investigations on a large scale, geodetic mass balance estimates from high resolution datasets with narrow swath widths such as from the TanDEM-X (TDM), Pléiades and WorldView satellite missions (Krieger et al., 2007; Gleyzes et al., 2012; Shean et al., 2016) would

* Corresponding author.

E-mail addresses: lukas.krieger@dlr.de (L. Krieger), dana.floricioiu@dlr.de (D. Floricioiu), niklas.neckel@awi.de (N. Neckel).

<https://doi.org/10.1016/j.rse.2019.111483>

Received 26 March 2019; Received in revised form 7 August 2019; Accepted 17 October 2019

0034-4257/ © 2019 The Authors. Published by Elsevier Inc. This is an open access article under the CC BY-NC-ND license (<http://creativecommons.org/licenses/by-nc-nd/4.0/>).

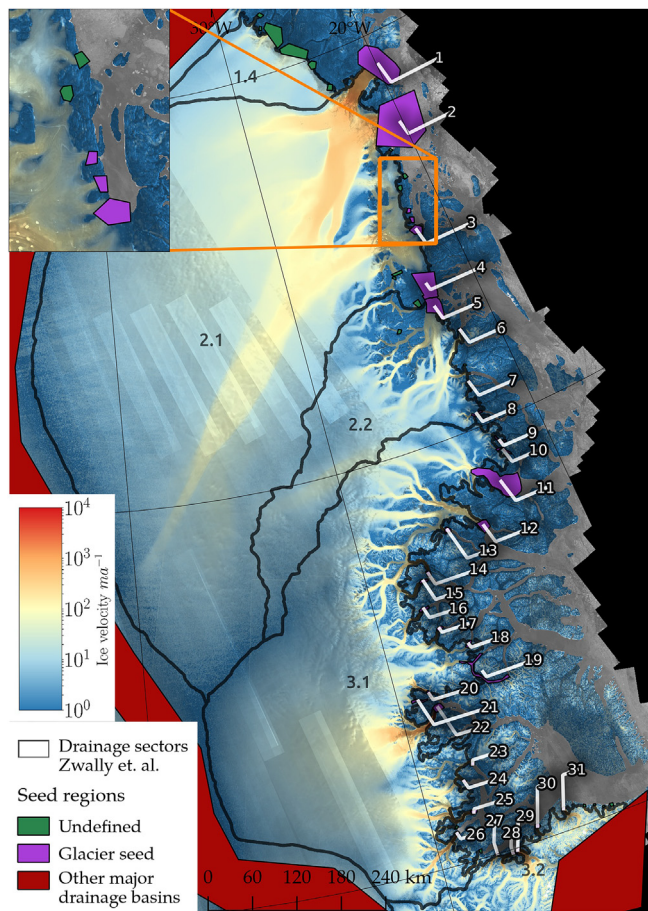


Fig. 1. The study site with 31 outlet glacier seed regions (magenta) of the basins listed in Table 1. Additional termini of small outlet glaciers or land terminating glaciers are marked as *undefined* seeds (green). Drainage to other major regions of Greenland is simulated by a rough outline around the Northeast Greenland sector (red). In the background the ice surface velocity map based on S1 (*GRIS-cci*) superimposed on the TDM global DEM backscattering mosaic. Black lines delineate the basins after Zwally et al. (2012).

benefit from individual glacier basins that allow a more focused data collection. Previously, Mouginit et al. (2015) delineated basins for Nioghalvfjærdsfjorden (79North) and Zachariæ Isstrøm by combining ice velocity and DEM information and Mouginit et al. (2019) applied a similar methodology to delineate the entire Greenland Ice Sheet into 260 individual drainage basins. Other authors report findings based on self assessed drainage basins in Greenland that were derived from watershed analysis assuming ice flow in the direction of the steepest slope (Felixson et al., 2017; Marzeion et al., 2012). However, the description of a detailed and fully traceable methodology for deriving basin inventories of individual outlet glaciers is still missing.

Recently available data products such as the TDM global DEM and ice sheet wide velocity measurements such as from Sentinel-1 can be employed to partition the glaciated area into individual catchments. In the following, we propose a method to delineate drainage basins for single outlet glaciers with a modified watershed algorithm based on ice surface velocity and DEM datasets.

2. Study site

The selected study site in Northeast Greenland is roughly equivalent to the drainage sectors 1.4, 2.1, 2.2, 3.1 and 3.2 as denoted by Zwally et al. (2012) or to the NE sector in the dataset produced by Mouginit et al. (2019). The area features marine-terminating outlet glaciers of different sizes including 79North with one of Greenland's rare ice

shelves. Another peculiar feature is the Northeast Greenland Ice Stream (NEGIS), that reaches over 700 km in the interior of the Greenland Ice Sheet and is drained by the outlet glaciers Zachariæ Isstrøm, 79North, Koføed-Hansen Bræ and Storstrømmen. The complex flow configurations of this region of the Greenland Ice Sheet with converging glaciers (L. Bistrup Bræ and Storstrømmen) as well as diverging ice flow (NEGIS into its individual outlet glaciers) present a challenging study site for the delineation of single glacier drainage basins. For the present work we selected 31 major, marine terminating outlet glaciers belonging to the Northeast part of the ice sheet (Fig. 1) and aimed at the generation of their individual catchments. The nomenclature and locations were adopted from Rignot and Mouginit (2012).

3. Datasets

We used two independent types of data to infer the flow direction of ice for the drainage basin delineation. The first data source is elevation information in the form of a rasterised DEM, which was employed with the assumption that ice flows in the direction of the steepest downhill slope. Ice velocity measurements were utilised as a second type of data to account for locations where the ice flow diverts from the direction given by the steepest slope. This can happen where the downhill flow is obstructed by large bedrock features or through interaction with other ice masses at glacier junctions (Van der Veen, 2013, Chapter 4.6). Overall, three independent DEMs and three different ice velocity maps were used to test the consistency of the drainage basin delineations.

3.1. Surface elevation datasets

The DEM used to delineate drainage basins is the TDM global DEM, which is assembled from time series of bistatic X-band InSAR acquisitions collected by the two twin satellites TerraSAR-X and TanDEM-X (Krieger et al., 2007). Over the Greenland Ice Sheet the data was acquired between 2011 and 2014 (Wessel et al., 2016). Subsequently, a single DEM was generated by averaging all available elevation measurements weighted with their estimated height errors (Zink et al., 2014). The TDM global DEM has a nominal pixel spacing of 0.4" (approx. 12 m) with an absolute vertical accuracy of 6.37 m given as 90% linear error over ice covered terrain (Rizzoli et al., 2017a). The DEM was chosen for the basin delineation application because of its high spatial resolution.

Two additional DEMs were used to test the consistency of the basin delineation. The first DEM used for the intercomparison is processed from Cryosat-2 (CS-2) data acquired in the period 2012–2013 and is posted on a regular grid of 1 km × 1 km pixel spacing (Helm et al., 2014). While the elevation bias due to penetration of TanDEM-X can be > 8 m in the interior of the ice sheet (Rizzoli et al., 2017b), only a slight bias of 0.2 ± 0.2 m is found over flat areas for CS-2 if an appropriate retracker is used (Schröder et al., 2017). The overall accuracy of the CS-2 DEM of Greenland is slope dependent but is given as 5 ± 65 m (Helm et al., 2014). The second DEM used for the intercomparison has been developed within the Greenland Ice Mapping Project (GIMP) (Howat et al., 2014). It was generated by merging elevation measurements including photogrammetry, laser- and radar altimetry. The DEM was calibrated to mean ICESat GLAS elevations acquired between 2003 and 2009 and has a posting of 90 m.

In the present work we did not investigate elevation changes that have occurred during the acquisition times of the DEMs and their possible impact on the drainage basin delineation. Instead the DEMs are assumed to represent accurate elevations of the ice sheet for their respective acquisition period. All DEMs were smoothed with a sliding average filter to remove longitudinal stresses and reduce the impact of local surface slope variations. The width of the filter kernel is determined according to multiples of the ice thickness at each point (Morlighem et al., 2017a). Kernel diameters of 20, 10 and 0 times the ice thickness have been picked to produce 3 different versions of each

DEM. For the remainder of the paper the versions are suffixed with *20H*, *10H* and *0H*. All results reported in our paper use *20H* as suggested in Paterson (2016, Chapter 8.7.2) while an additional example of the smoothing kernel effect on the basin delineation is given in the Supplement (Fig. S1).

3.2. Ice velocity datasets

To supplement surface elevation data, we used surface velocity derived through offset tracking of Sentinel-1 (S-1) SAR amplitude backscattering images. A multi-annual Sentinel-1 ice velocity map of Greenland was produced within the Greenland Ice Sheet project of ESA's Climate Change Initiative (GrIS-cci) Programme (Nagler et al., 2015). We obtained the geocoded velocity product for the time period Oct. 2014–Apr. 2019 and used velocity components with a posting of 250 m that we term *GrIS-cci* velocities.

We employed two additional surface velocity datasets to compare the resulting drainage basins. The first of these velocity maps was also derived by Sentinel-1 offset tracking and incorporates 2607 image pairs acquired over Northeast Greenland during the winters of 2016, 2017 and 2018. The processing includes mosaicking of S-1 TOPS burst SLC data, co-registration between 6-day repeat passes based on precise orbit information, offset estimation in range and azimuth direction, a projection into a polar stereographic coordinate system assuming surface parallel ice flow and a three step filtering procedure (Lüttig et al., 2017). The final mosaic is posted at 250 m and small data gaps are filled via an inverse distance interpolation scheme. In the following this velocity field is denoted as *AWI-S1* velocities. Note that *AWI-S1* velocities and *GrIS-cci* are partially based on the same S-1 acquisitions but were processed separately. The second additional ice velocity dataset used in the intercomparison is distributed within the MEaSUREs project (Joughin et al., 2016). This velocity map has been generated by combining speckle- and feature tracking techniques applied at the ice sheet margins together with InSAR measurements for the ice sheet interior. The used acquisitions fall within the time of 1995 and 2015 and stem from multiple SAR sensors (ERS-1/2, RADARSAT, ALOS, TerraSAR-X) as well as Landsat 8. The MEaSUREs product is also posted at 250 m (Joughin et al., 2017).

3.3. Ice classification mask

In order to restrict the processing to the ice sheet area we used the Land Ice and Ocean Classification Mask product of the MEaSUREs GIMP project (Howat et al., 2014). This data set provides a complete land ice, ice free terrain and ocean classification mask for the Greenland Ice Sheet that was mapped using a combination of Landsat 7 ETM+ panchromatic band imagery and RADARSAT-1 SAR amplitude images acquired between 1999 and 2002. We modified the IceMask layer of the product which includes the ice shelves by eliminating the small ice caps and glaciers at the Greenland periphery that are not connected to the ice sheet and applied the watershed processing to the remaining ice coverage.

3.4. Selection of seed regions

Seed locations are required for each catchment in order to start the partitioning of the ice sheet into drainage basins. The seed regions are defined on the ice of the termini marking areas upstream from the glacier front. Thus the seed regions belong to the part of the tongue where ice is discharged into the ocean or where the glacier is terminating on land. The largest seed regions for the study site are visualized in Fig. 1. We have defined three types of seed regions needed to support our processing: (1) on each terminus of the 31 marine terminating glaciers considered for catchment delineation (2) several seed regions of small unnamed glaciers that flow also to the ice sheet margin and (3) a large one located along the ice divides outside the rough outline of the

complete Northeast Greenland drainage region. Regions of type (1) and (2) act as sinks in the ice sheet's flow system, while region (3) simulates the glaciers draining into the adjacent West and Southeast Greenland regions.

4. Methods

For the delineation of individual glacier catchment areas, a classical flood-filling watershed algorithm (Beucher et al., 1992) was adapted to use both elevation and ice velocity data. In this way, we aim at a more reliable separation of glaciers in fast moving areas than by utilising only a DEM. All datasets were resampled to the same grid of 250 m pixel spacing by a cubic spline interpolation before the start of the processing, which inherently specifies the pixel spacing at which the independent parts of the algorithm operate.

4.1. Watershed algorithm

The watershed algorithm is an image processing transformation whose name refers to the geological watershed and which is widely used for various image segmentation purposes (Sonka et al., 2014, Chapter 6.3.4). When operating on a DEM and associated seed points, the watershed algorithm finds the lines separating adjacent drainage basins (Beucher et al., 1992; Vincent and Soille, 1991). We used an implementation of the watershed algorithm which utilises a priority queue that is sorted by minimum elevation (Barnes et al., 2014). During the algorithm run, pixels adjacent to each seed point are entered into the queue and are processed in the order of increasing elevation. This ensures a pixel-wise processing, with regions evolving from given seed points to form a partitioning of the area of interest. Finally, the drainage divides of the DEM are represented by the boundaries of the basins generated by the watershed algorithm.

One approach to delineate basins is to apply the watershed algorithm only on the ice sheet DEM and the seeds corresponding to its outlet glaciers. However, Rignot et al. (2000) point out that in order to correctly delineate catchments in fast moving areas, ice surface velocities must be taken into account in addition to the slope information provided by the DEM. As directional errors in the velocity measurements are more related to the velocity magnitude than to absolute elevation, we adopted a method similar to Mouginot et al. (2015) which uses thresholds for the ice velocity magnitude to separate between ice flow and surface slope direction instead.

4.2. Streamline calculation

In order to accommodate velocity information in the traditional watershed algorithm, we calculated streamlines from the north and east velocity components. They describe the trajectory that imaginary particles would take in the given velocity field. We produced discrete streamlines with the procedure described by Cabral and Leedom (1993) but restricted the calculation to areas moving faster than a given absolute velocity threshold, while slower areas were discarded. The streamline computation is included in the modified watershed algorithm starting from a given pixel and ending once the streamline extends beyond the coverage of the velocity field or if the streamline merges with an already existing one. An example for the NEGIS sector is depicted in Fig. 2.

4.3. Catchment delineation

To combine the directional information from ice flow with the slope information, the traditional watershed algorithm was modified to disregard slope information in areas of fast moving ice where the velocity magnitude exceeds a pre-defined threshold. Instead, every time such an area is encountered, the entire labelled flow line (as derived in section 4.2) is included in the currently processed drainage area and its entire

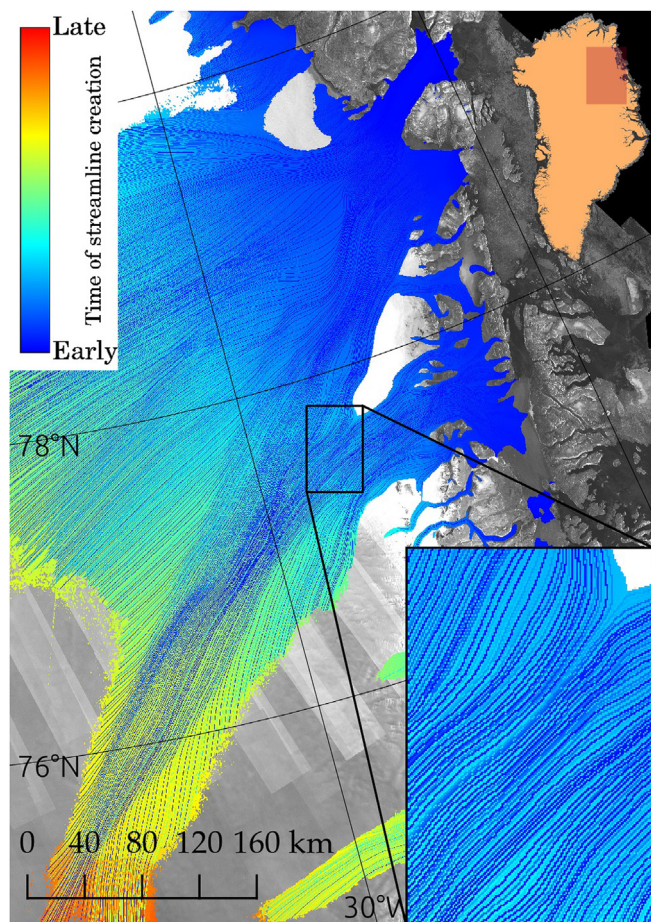


Fig. 2. The streamlines for the NEGIS drainage sector colour coded by the time of creation during the modified watershed algorithm. The streamlines have been calculated on the complete averaged *GrIS-cci* velocity dataset for ice speeds exceeding 13.67 m a^{-1} . Dark-blue refers to streamlines originating from low altitudes close to the coast propagating to the upper part of NEGIS. Light-blue to red colours are associated to streamlines starting at higher elevations. The inset shows streamlines clearly separating NEGIS into two arms. In the background the TDM SAR backscattering amplitude mosaic.

neighbourhood is entered in the priority queue of the watershed algorithm.

The choice of seed regions controls the partitioning of the ice-covered area into drainage basins. A catchment was generated for every seed region of type (1) (Section 3.4) with a unique seed label. This partitions the entire glaciated area into a number of basins equal to the number of different seed region labels. All additional smaller glaciers of type (2) and the adjacent major drainage region (3) were assigned the *undefined* label. If an additional drainage basin is desired in a part of the ice sheet that drains through an *undefined* seed region of type (2), an additional labelled outlet glacier seed (1) can be placed and the modified watershed algorithm can be re-run.

In order to mitigate the propagation of local errors in the datasets to global errors in the drainage delineation we applied a Monte-Carlo method adding Gaussian noise with zero mean to both the DEM and the ice velocity components as well as the used ice velocity threshold. In this setting $N = 10000$ runs of the algorithm were performed using the pixel-wise uncertainties for the x and y ice velocity components. The standard deviation for the DEM and ice velocity threshold were set to $\sigma_{DEM} = 10 \text{ m}$ and $\sigma_i = 2 \text{ m a}^{-1}$, respectively. Subsequently, each pixel was assigned the basin label of maximal occurrence in all runs and a probability measurement was calculated based on the percentage of total Monte-Carlo runs for which that pixel was included in that

particular basin. Noisy delineations at the basin boundaries were cleaned by restricting the number of connected clusters per label to 1.

5. Selection of the ice velocity magnitude threshold

For slow moving ice, the reduced SNR in the amplitude correlation functions of the speckle tracking measurements can lead to a degradation of the flow direction estimate. Additionally, there are artefacts in the velocity measurement stemming from an active ionosphere. Even though the velocity vector can be measured more precisely with InSAR and higher quality velocity maps with smaller flow direction uncertainties can be produced, small scale ionospheric perturbations still remain in the velocity measurements after the ionospheric correction by the split-spectrum method (Gomba et al., 2016, 2017). At the ice divides, the errors of the velocity components are in the order of 5 m a^{-1} . In these areas, the direction of the steepest surface slope can be derived more accurately as long as the assumption of downhill flow along smoothed DEMs is valid. On the other end of the velocity range, fast moving ice does not always flow in the direction of the steepest slope if there exists an instability or flow change. Here, the actual flow direction can be precisely derived from the offset tracking results. By using flow directions instead of slope information and vice versa in regions of high and low ice velocities, the drawbacks of both types of data can be overcome.

The criterion whether the slope-based or velocity-based flow directions should be utilised was predicated on the comparison between two angles. Both types of flow directions were expressed as vectors with unit length and the angular argument was used. The ice flow angle given by *GrIS-cci* velocities and the aspect angle (direction of steepest slope) of the TDM global DEM were computed over the entire Northeast Greenland region. The mean difference between these angles as well as their correlation are calculated over velocity magnitude bins that contain an equal number of points (Fig. 3a). The velocity of 13.67 m a^{-1} at maximum correlation was chosen as the threshold for the modified

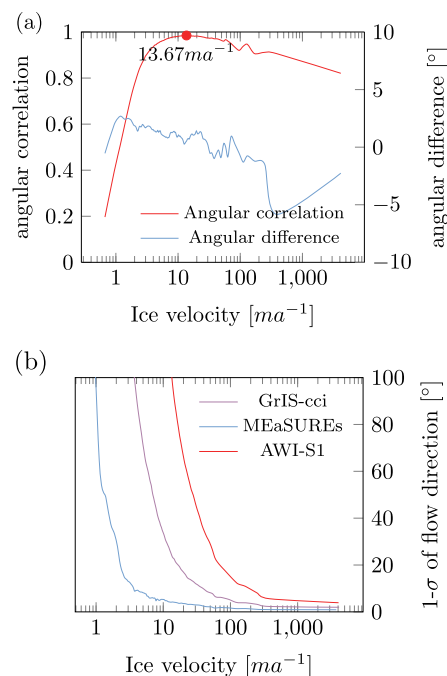


Fig. 3. (a) Correlation and mean difference of the TanDEM-X global DEM aspect angle (direction of steepest slope) and the flow angle of *GrIS-cci* velocity vectors. The comparison is carried out over the entire Northeast Greenland ice sheet area for velocity bins that contain an equal number of points. At a velocity of 13.67 m a^{-1} the maximum correlation is reached (red dot). (b) The uncertainty of the flow direction for the 3 different velocity maps.

watershed algorithm indicating the use of DEM or ice velocities. Above 13.67 m a^{-1} we expect the direction from velocity information to be accurate to the true ice flow direction and below the threshold the slope information is trusted. Fig. 3b shows this degradation of the flow direction measurement with decreasing ice velocity magnitude.

For the TDM global DEM and *GrIS-cci* velocity combination the angle correlation reaches a maximum of 0.98 while the mean difference of the two angles is 0.5° at this peak. Angle differences up to 6° occur in regions of fast and slow ice movement. For fast flowing ice ($> 300 \text{ m a}^{-1}$) correlation of approx. 0.85 is found while slower ice ($< 2 \text{ m a}^{-1}$) has correlation values of less than 0.6 indicating a misalignment between the ice flow and surface slope directions. It should be noted that the correlation stays close to 1 in a broad range of velocities, indicating that the exact threshold can be variable and plays a limited role in the basin delineation.

The angle analysis was performed for the different DEM and velocity dataset combinations, yielding similar results with correlation patterns peaking between 13 m a^{-1} and 44 m a^{-1} (Supplement, Fig. S2). For the InSAR-based velocity map, correlations close to 1 are maintained for slower ice velocities even though the highest angle correlations are still found between 10 m a^{-1} and 44 m a^{-1} . We applied the respective velocity thresholds for the different input dataset combinations and modified the threshold by adding Gaussian noise for each individual Monte-Carlo run. This limits the dependence of the exact threshold on the delineation.

6. Results

We used the combination TDM global DEM 20H and *Gr-IS-cci* velocities with 250m pixel spacing as input dataset for the modified watershed algorithm and seed regions for its initialization. The resulting delineations of the 31 drainage basins are shown in Fig. 4a. The streamline calculation performed during the algorithm runs over areas where the ice velocity exceeds the previously estimated threshold (TDM-GrIS-cci: 13.67 m a^{-1}). The probability estimates for each assigned basin label resulting from the Monte-Carlo simulation with $N = 10000$ runs are shown in Fig. 4b. The characteristics of the generated basins are summarised in Table 1 in decreasing order of their

drainage area.

7. Intercomparison with other DEM and velocity products

Additional to the results presented above, basin delineations with all other input data combinations of the DEMs (TDM, GIMP, CS-2) and ice velocities (GrIS-cci, MEaSURES, AWI-S1) were generated for inter-comparison purposes. This way we gain insight if the errors that are inherent to each dataset have an effect on our proposed delineation.

In order to quantify the similarity between the results based on different datasets, we calculate the Jaccard index J for each combination of two drainage basin delineation results $A = \{A_1, A_2, \dots, A_n\}$ and $B = \{B_1, B_2, \dots, B_n\}$ (Jaccard, 1912). Over the whole region of interest we divide the number of commonly labelled pixels in both delineations by the overall number of labelled pixels. A_k, B_k are therefore holding all pixels labelled for glacier k and $|\dots|$ denotes the number of pixels in the given set. The Jaccard index is 1 if A and B delineations are in perfect agreement and decreases with their spatial dissimilarity.

$$J = \frac{\left| \bigcup_{k=1}^n A_k \cap B_k \right|}{|A \cup B|} \quad (1)$$

The Jaccard indices of the various input data combinations range from 0.81 to 0.98 (Table 2). Discrepancies in the delineation of the basin boundaries are visible in Fig. 5 and are due to different time spans, error sources and limitations of each of the input data products. All delineations using the GIMP DEM perform closer to that of the TDM global DEM compared to those using the CS-2 DEM. The lower Jaccard index of 0.90 when comparing catchment delineations based on the TDM global DEM to the ones based on CS-2 (both using *GrIS-cci* velocities) is caused by the low resolution and poor performance of CS-2 in areas of complex topography at the margin of the Greenland Ice Sheet (Fig. 5 b,c). As the flood-filling watershed algorithm processes the margins early in the labelling process, errors can propagate towards the interior of the ice sheet and the final difference in basin area can be substantial. The results using the GIMP DEM are in better agreement (Jaccard index 0.98) with the TDM global DEM based basins (both using *GrIS-cci* velocities) since the resolution of both products is high

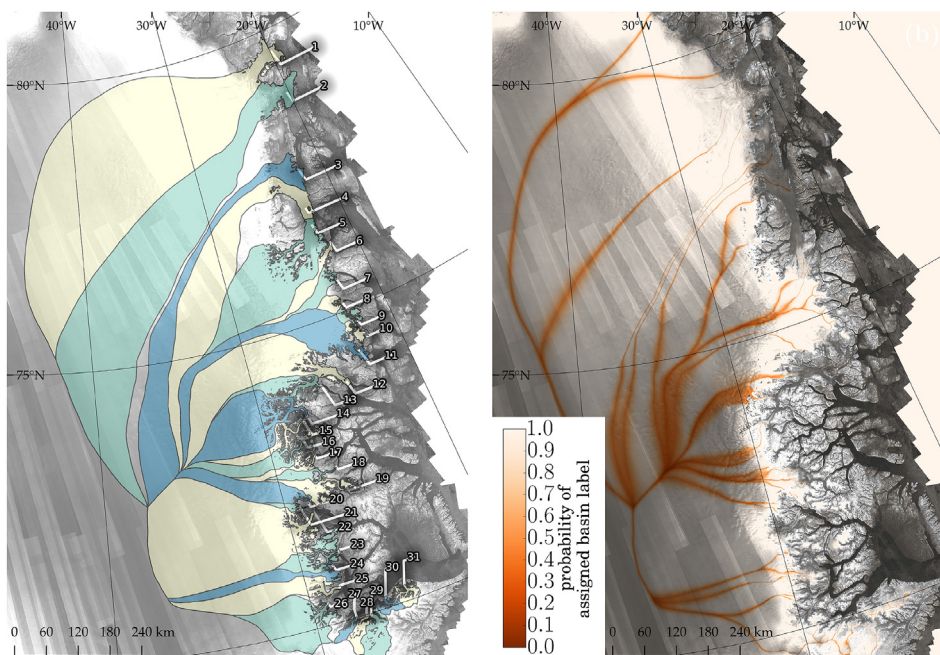


Fig. 4. (a) Northeast Greenland Ice Sheet region divided into drainage basins of the 31 outlet glaciers in Table 1. (b) The pixel-wise probability of the assigned basin label for each basin. In the background the SAR backscattering amplitude layer of the TDM global DEM.

Table 1

Drainage basin areas \mathcal{A} for each numbered glacier as in Fig. 1 based on the TDM-GrIS-cci input dataset combination. The ice volume \mathcal{V} is calculated with the Bedmachine dataset (Morlighem et al., 2017a, b). Area fractions \mathcal{A}_{frac} are given with respect to the total Greenland Ice Sheet area (Howat et al., 2014). Minimum and maximum area \mathcal{A}_{min} and \mathcal{A}_{max} for a basin are given based on the extrema in the delineations resulting from all other input dataset combinations. Area differences $\Delta\mathcal{A}$ are reported for corresponding catchments in Mouginot et al. (2019) and sea level equivalents (SLE) were calculated.

#	Glacier name	\mathcal{A} [km ²]	\mathcal{A}_{frac} [%]	\mathcal{A}_{min} [km ²]	\mathcal{A}_{max} [km ²]	\mathcal{V} [km ³]	$\Delta\mathcal{A}$ [km ²]	SLE [m]
1	Nioghalfjersfjorden (79North)	107791	6.28	107774	111884	227424	-2559	0.58
2	Zachariæ Isstrøm	84398	4.92	83879	96547	200199	-6864	0.51
3	Kofoed-Hansen Bræ	74686	4.35	45057	90473	173136	-	0.44
22	Daugaard-Jensen	48369	2.82	47847	51225	110810	-1557	0.28
4	Storstrømmen	28859	1.68	23353	37444	53872	-	0.14
12	Waltershausen Gletscher	23141	1.35	17354	25490	34821	-990	0.09
5	L. Bistrup Bræ	21868	1.27	21652	29701	24648	233	0.06
14	Gerard de Geer Gletscher	15735	0.92	11965	19903	19932	2267	0.05
11	Wordie Gletscher	14995	0.87	10240	17774	21686	4771	0.05
26	Vestfjord Gletscher	11806	0.69	11285	13082	11506	590	0.03
25	Rolige Gletscher	9917	0.58	9146	12172	18003	-	0.05
20	F. Graae Gletscher	7288	0.42	37	7525	12754	1781	0.03
16	Nordenskiöld Gletscher	5209	0.30	1006	5545	6967	1132	0.02
24	Unnamed Hare Fjord	5170	0.30	1375	6189	9683	-	0.02
13	Adolf Hoel Gletscher	4323	0.25	2577	7798	1845	-4773	0.00
15	Jættegletscher	3819	0.22	1158	5407	3154	-1710	0.01
29	Magga Dan Gletscher	3768	0.22	3582	4015	2120	-672	0.01
23	Eielson Gletscher	3700	0.22	2555	5083	1404	-	0.00
19	Violingletscher	3432	0.20	760	3432	1162	-	0.00
6	Soranerbræen Gletscher	2956	0.17	2545	5586	2655	-	0.01
7	Einar Mikkelsen Gletscher	2263	0.13	23	2263	1597	-	0.00
17	Hisinger Gletscher	1939	0.11	1939	15897	1568	-932	0.00
18	Wahlenberg Gletscher	1559	0.09	1079	1699	988	-	0.00
31	Bredegletscher	1546	0.09	1485	1690	254	276	0.00
28	Kista Dan Gletscher	1524	0.09	822	1585	934	-	0.00
8	Heinkel Gletscher	1093	0.06	253	1100	417	-	0.00
30	Sydbræ	1072	0.06	997	1091	148	-93	0.00
27	Unnamed Vestfjord S	931	0.05	798	1308	250	-	0.00
9	Tvegegletscher	924	0.05	771	960	130	-	0.00
10	Pasterze	743	0.04	715	761	16	-	0.00
21	Charcot Gletscher	580	0.03	560	728	360	-572	0.00

enough to capture topographic details in steep areas. An area of 9% of all basins in the sector is labelled differently when substituting GrIS-cci with the MEaSURES velocity dataset, whereas the AWI-S1 velocities show dissimilarities of 11% to the TDM-GrIS-cci result. In general it can also be observed that greatest discrepancies between the datasets in Fig. 5a are located in the basins that are delineated with low probabilities in Fig. 4b.

Smoothing the DEM before watershed processing has less impact than the selection of different input datasets. The lowest Jaccard index for delineations with 10H average kernels is 0.94 while no smoothing shows a minimum Jaccard index of 0.90 (Table 3). A decreasing trend of basin similarities with smaller smoothing kernels can be observed for each combination of input datasets. Without smoothing the TDM global DEM, the resulting discrepancies are 6% of the area compared to the presented delineation using a smoothing kernel of 20H.

Table 2

Jaccard indices for all combinations of input DEMs and ice velocity datasets compared to the basins based on the TanDEM-X global DEM and the GrIS-cci velocities. The comparison is always performed with respect to delineation results applying the same DEM smoothing kernel with sizes equal to multiples of the ice thickness (20H, 10H, 0H).

Drainage basin delineation identifier	Input DEM & IV dataset combinations								
	TDM			GIMP			CS-2		
	GrIS-cci	MEaSURES	AWI-S1	GrIS-cci	MEaSURES	AWI-S1	GrIS-cci	MEaSURES	AWI-S1
TDM-GrIS-cci-20H	1.00	0.91	0.89	0.98	0.89	0.89	0.90	0.87	0.84
TDM-GrIS-cci-10H	1.00	0.91	0.89	0.98	0.85	0.87	0.90	0.87	0.83
TDM-GrIS-cci-0H	1.00	0.93	0.88	0.96	0.84	0.85	0.88	0.87	0.81

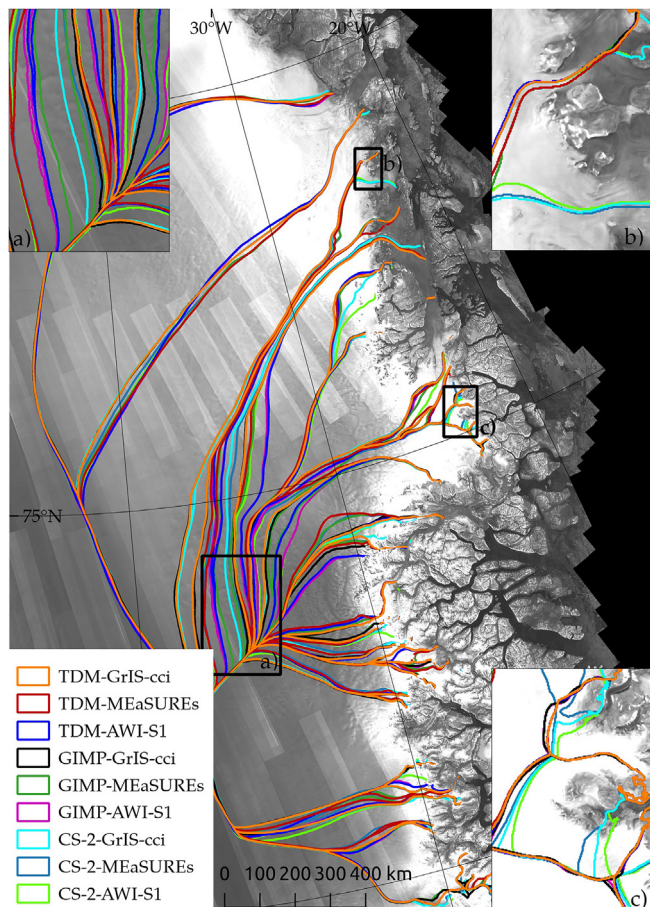


Fig. 5. The basin boundaries resulting from all input DEM and velocity dataset combinations. Inset (a): different delineations that originate from diverging ice flow directions at lower elevations. (b) and (c): places where CS-2 delineations are at different locations than the GIMP and TDM based boundaries. In the background the TDM SAR backscattering amplitude mosaic.

the ice stream is misclassified. One has to note that including ice flow direction allows to delineate drainage basins for the current state of the ice sheet and in this setting the classical watershed processing fails to properly delineate the catchments. However, using current ice velocities does not allow to delineate retroactively the drainage basins for a past ice sheet in balanced state, since the velocity patterns change in response to ice sheet imbalances. Nonetheless, using only a smoothed DEM assumes an ice sheet in balance which is not the case for the recent DEMs and the basins boundaries may differ substantially (Supplement, Fig. S3). If instead of ice flow catchments the research objective are basins for surface water routing, one must use an unfiltered, high resolution DEM only, ignore ice velocity and include land areas in the processing.

The choice of seed regions is an important step for the creation of drainage basins, because it has a direct impact on their delineation. This effect can be observed at the additional *undefined* seeds (Fig. 1), which

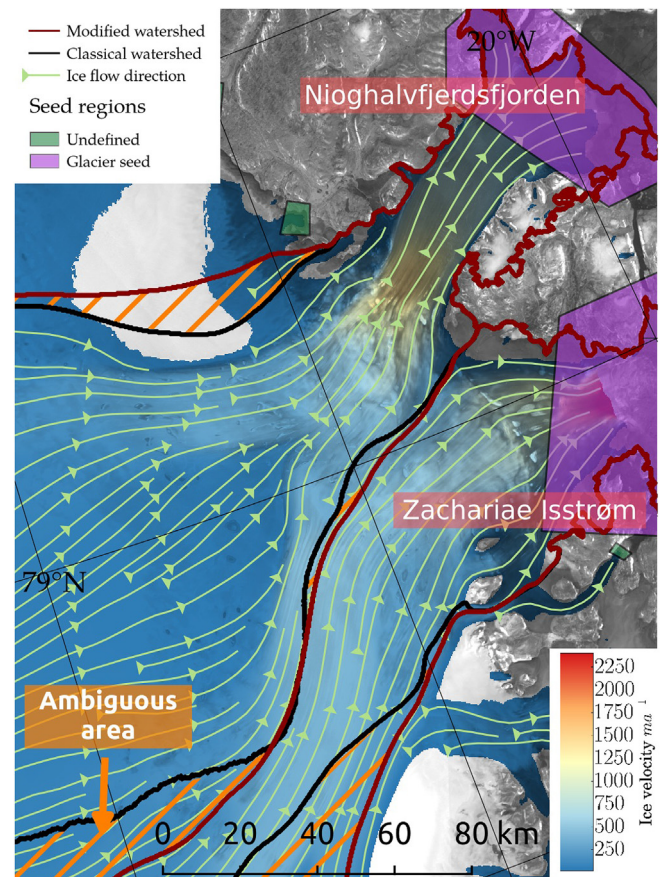


Fig. 6. Watershed lines separating the two glaciers 79North and Zachariae Isstrøm derived by the classical watershed algorithm based solely on DEM information (black line) compared to the basin boundary when additional ice velocity is used (red line). The disagreement between the drainage divides leads to an ambiguous area which according to the ice flow direction (green arrows) is misclassified by the classical watershed procedure. In the background the TDM SAR backscattering amplitude mosaic.

effectively exclude areas from the drainage delineation that are not directly drained through one of the selected outlet glaciers of type (1). In Fig. 6 one such example is shown adjacent to the 79North basin. Changing the extent of this seed region has the potential to alter the entire 79North basin area by thousands of km². The same problem exists for all adjoining seed regions located directly at the ice margin where the ice/land interface has to be manually distributed to the neighbouring glaciers. Because the processing was restricted to the glaciated area only and most of the seed regions are located in clearly separated fjords this is a minor problem for large parts of the ice sheet. Here, the shape of the seed polygons has no effect on the delineation. Setting the seed regions requires a decision on which outlet glaciers should be assigned to a common drainage system. If in doubt we advise to create separate seed regions for the glaciers in question with the possibility to merge the basins retroactively. Similarly, if glacial surges

Table 3

Jaccard indices for the comparison of drainage basin delineations using the DEM smoothed with the 20H kernel versus the 10H smoothed and 0H (original) DEM.

DEM smoothing kernel size	Input DEM & IV dataset combinations (20H)								
	TDM			GIMP			CS-2		
	GrIS-cci	MEaSURES	AWI-S1	GrIS-cci	MEaSURES	AWI-S1	GrIS-cci	MEaSURES	AWI-S1
10H	0.98	0.98	0.96	0.97	0.94	0.96	0.98	0.99	0.97
0H	0.94	0.93	0.90	0.94	0.90	0.91	0.96	0.97	0.93

are suspected, questionable basins should also be combined after the watershed delineation using insight from the accompanying probability estimates.

Apart from the seed selection, the implementation of the flood-filling watershed algorithm is deterministic and the errors of the basin delineation are a result of errors in the input data. In flood-filling watershed algorithms, localised errors of the input dataset can propagate to global errors in the final segmentation. It is therefore challenging to quantify the quality of the drainage basin delineations directly from the local, pixel-wise uncertainties of the input data (Straehle et al., 2012). Instead, we investigate the uncertainty of the basin boundaries by performing Monte-Carlo experiments using standard deviations reported for the 3 individual velocity maps. In the case of the DEM, the uncertainties are difficult to evaluate because of the ice thickness dependent smoothing. σ_{DEM} was set conservatively and likely exceeds the expected error in the DEM datasets. The reported probability map for the basins therefore represents an upper boundary. Additionally, a small uncertainty of $\sigma_t = 2ma^{-1}$ was applied to the velocity threshold derived in section 5 to limit its effect on the delineation.

While the overall height accuracy of the TDM global DEM is given with 3.49 m it decreases to 6.37 m over ice covered regions (Rizzoli et al., 2017a). This effect can be attributed to the SAR signal penetration. In the interior of the Greenland Ice Sheet the penetration bias at X-band compared to ICESat measurements can be > 8 m with a mean elevation bias of 5.4 m for the dry snow zone (Rizzoli et al., 2017b). However, the rather gradual spatial variability of the penetration bias implies a very small effect on the relative height accuracy at regional scale and the related delineation of ice divides. Nevertheless, with the presented methodology it is also possible to use merged DEM information from different sources like the TDM global DEM at lower elevations combined with CS-2 elevations for the interior of the ice sheet to minimize possible effects of the penetration bias. When performing this scenario with substituted TDM elevations above 2000 m no major differences have been found to using only TDM elevations (Jacard index of 0.99, Supplement, Fig. S4).

Similar results are found when the modified watershed algorithm is run with surface velocity fields produced by different groups (Table 2). However, it should be noted that here we rely on multi year averages in order to increase the accuracy of the speckle tracking results in slowly moving areas.

Overall, the catchment area results in Table 1 show differences to the values found in the literature. According to our findings, the glacier catchments of 79North and Zachariæ Isstrøm are 2559 km² and 6864 km² smaller compared to the corresponding basins in Mougnot et al. (2019) after correcting for the different seaward basin extent. Relative to the total basin area, larger discrepancies are found for Wordie Gletscher (32%) or Adolf Hoel Gletscher (110%). Two large basins of the surge-type Storstrømmen and Kofoed-Hansen Bræ are not included in the comparison because their catchments are combined in Mougnot et al. (2019). The discrepancies can arise for various reasons, including the choice of the DEM, the velocity dataset or the used methodology. Moreover, a clear definition is needed for the points of drainage to land and ocean, i.e. our seed regions. The mentioned sources do not describe the methodology in detail. The present study based on independent datasets can reliably delineate basins of certain glaciers like in the case of 79North where the maximal area discrepancy ($A_{max} - A_{min}$) of all input dataset combinations is only 4110 km² (0.4%) (Table 1). 79North shows clearly defined basin boundaries with low variability. Other catchments however (e.g. Storstrømmen and Kofoed-Hansen Bræ), are derived with low probability (Fig. 4b).

9. Conclusion

Individual glacier catchments support a quantification of glacier changes for a specified region and are therefore an important tool in the field of glaciology and hydrology. Moreover, standardised basins allow

for a direct comparison of study results and lead to more robust estimates of glacier mass balances. We developed a method based on objective decision criteria for tracing basin outlines and applied it for the Northeast Greenland region. By using combined DEM and velocity information with a modified watershed algorithm, a new partitioning of the region into 31 individual glacier catchments has been performed. As an independent, high accuracy data base for full validation of the results is lacking, quality assessment was supported by performing an intercomparison with different input data combinations of DEMs and ice velocity products showing discrepancies of up to 16% in the extent of the catchment areas. The quality of the presented results was further assessed by a probability measure from additional Monte-Carlo experiments. Compared to watershed delineations using only a DEM, there are however major differences in reported drainage areas for certain glaciers, showing that previous approaches on ice sheets delivered different basin boundaries not fully matching the present day ice sheet conditions. We suggest that catchment delineations from DEMs have to be supported by ice velocity maps and seed regions. Given high resolution elevation measurements like the TanDEM-X global DEM and ice sheet wide ice velocity data like those provided by Sentinel-1 as well as basin starting points, the developed method has the potential to produce fully traceable outlines of drainage basins for entire Greenland and Antarctica. As ice sheet velocities are known to experience seasonal or multiyear variations, there is a possibility that also drainage areas are affected by such changes. Therefore, repeated investigations of glacier drainage systems should be carried out in the future with multi-temporal velocity datasets and accurate, high-resolution DEMs. Moreover, the procedure is also directly applicable on smaller scales for the delineation of ice divides between outlet glaciers of ice caps and ice fields. It can be used to refine and update glacier inventories like the Randolph Glacier Inventory, e.g. by adding separate basins for each glacier on continuous ice bodies (RGI Consortium, 2017).

Acknowledgements

This research was supported by the Deutsche Forschungsgemeinschaft (DFG, FL 848/1-1). N.N. has received funding from the European Union's Horizon 2020 research and innovation programme under grant agreement No 689443 via project iCUPE (Integrative and Comprehensive Understanding on Polar Environments). The TanDEM-X global DEM tiles were provided by DLR under the research proposal DEM_GLAC0671 ©DLR 2017. We thank ENVEO GmbH for providing the multi-annual ice velocity map.

Appendix A. Supplementary data

Supplementary data to this article can be found online at <https://doi.org/10.1016/j.rse.2019.111483>.

References

- Barnes, R., Lehman, C., Mulla, D., 2014. Priority-flood: an optimal depression-filling and watershed-labeling algorithm for digital elevation models. *Comput. Geosci.* 62, 117–127.
- Beucher, S., et al., 1992. The watershed transformation applied to image segmentation. *Scanning Microsc. Suppl.* 299–299.
- Cabral, B., Leedom, L.C., 1993. Imaging vector fields using line integral convolution. In: *Proceedings of the 20th Annual Conference on Computer Graphics and Interactive Techniques*, pp. 263–270 ACM.
- Felikson, D., Bartholomäus, T.C., Catania, G.A., Korsgaard, N.J., Kjær, K.H., Morlighem, M., Noël, B., Van Den Broeke, M., Stearns, L.A., Shroyer, E.L., et al., 2017. Inland thinning on the Greenland ice sheet controlled by outlet glacier geometry. *Nat. Geosci.* 10, 366.
- Gleyzes, M.A., Perret, L., Kubik, P., 2012. Pleiades system architecture and main performances. *Int. Arch. Photogr. Remote Sens. Spat. Inf. Sci.* 39, 537–542.
- Gomba, G., Parizzi, A., De Zan, F., Eineder, M., Bamler, R., 2016. Toward operational compensation of ionospheric effects in SAR interferograms: the split-spectrum method. *IEEE Trans. Geosci. Remote Sens.* 54, 1446–1461.
- Gomba, G., Rodríguez González, F., De Zan, F., 2017. Ionospheric phase screen

- compensation for the Sentinel-1 TOPS and ALOS-2 ScanSAR modes. *IEEE Trans. Geosci. Remote Sens.* 55, 223–235.
- Groh, A., Ewert, H., Rosenau, R., Fagioli, E., Gruber, C., Floricioiu, D., Abdel Jaber, W., Linow, S., Flechtner, F., Eineder, M., et al., 2014. Mass, volume and velocity of the Antarctic Ice Sheet: present-day changes and error effects. *Surv. Geophys.* 35, 1481–1505.
- Hardy, R., Bamber, J., Orford, S., 2000. The delineation of drainage basins on the Greenland ice sheet for mass-balance analyses using a combined modelling and geographical information system approach. *Hydrol. Process.* 14, 1931–1941.
- Helm, V., Humbert, A., Miller, H., 2014. Elevation and elevation change of Greenland and Antarctica derived from CryoSat-2. *Cryosphere* 8, 1539–1559.
- Howat, I.M., Negrete, A., Smith, B., 2014. The Greenland Ice Mapping Project (GIMP) land classification and surface elevation data sets. *Cryosphere* 8, 1509–1518.
- Jaccard, P., 1912. The distribution of the flora in the alpine zone. *New Phytol.* 11, 37–50.
- Joughin, I., Smith, B.E., Howat, I.M., 2017. A complete map of Greenland ice velocity derived from satellite data collected over 20 years. *J. Glaciol.* 1–11.
- Joughin, I., Smith, B.E., Howat, I.M., Scambos, T.A., 2016. MEASURES Multi-Year Greenland Ice Sheet Velocity Mosaic, Version 1. Boulder, Colorado USA. NASA National Snow and Ice Data Center Distributed Active Archive Center.
- King, M.D., Howat, I.M., Jeong, S., Noh, M.J., Wouters, B., Noël, B., van den Broeke, M.R., 2018. Seasonal to decadal variability in ice discharge from the Greenland Ice Sheet. *Cryosphere* 12, 3813–3825. <https://doi.org/10.5194/tc-12-3813-2018>.
- Krieger, G., Moreira, A., Fiedler, H., Hajnsek, I., Werner, M., Younis, M., Zink, M., 2007. TanDEM-X: a satellite formation for high-resolution SAR interferometry. *IEEE Trans. Geosci. Remote Sens.* 45, 3317–3341.
- Lewis, S.M., Smith, L.C., 2009. Hydrologic drainage of the Greenland ice sheet. *Hydrol. Process.* 23, 2004–2011.
- Lüttig, C., Neckel, N., Humbert, A., 2017. A combined approach for filtering ice surface velocity fields derived from remote sensing methods. *Remote Sens.* 9, 1062.
- Marzeion, B., Jarosch, A., Hofer, M., 2012. Past and future sea-level change from the surface mass balance of glaciers. *Cryosphere* 6, 1295–1322.
- Morlighem, M., Williams, C.N., Rignot, E., An, L., Arndt, J.E., Bamber, J.L., Catania, G., Chauché, N., Dowdeswell, J.A., Dorschel, B., et al., 2017a. Bedmachine v3: complete bed topography and ocean bathymetry mapping of Greenland from multibeam echo sounding combined with mass conservation. *Geophys. Res. Lett.* 44.
- Morlighem, M., Williams, C.N., Rignot, E., An, L., Arndt, J.E., Bamber, J.L., Catania, G., Chauché, N., Dowdeswell, J.A., Dorschel, B., et al., 2017b. Ice Bridge Bed Machine Greenland, Version 3. Boulder, Colorado USA. NASA National Snow and Ice Data Center Distributed Active Archive Center.
- Mouginot, J., Rignot, E., Björk, A.A., van den Broeke, M., Millan, R., Morlighem, M., Noël, B., Scheuchl, B., Wood, M., 2019. Forty-six years of Greenland Ice Sheet mass balance from 1972 to 2018. *Proc. Natl. Acad. Sci.* 116, 9239–9244. <https://doi.org/10.1073/pnas.1904242116>. URL: <https://www.pnas.org/content/116/19/9239>.
- Mouginot, J., Rignot, E., Scheuchl, B., Fenty, I., Khazendar, A., Morlighem, M., Buzzi, A., Paden, J., 2015. Fast retreat of Zachariæ Isstrøm, northeast Greenland. *Science* 350, 1357–1361.
- Nagler, T., Rott, H., Hetzenecker, M., Wuite, J., Potin, P., 2015. The Sentinel-1 mission: new opportunities for ice sheet observations. *Remote Sens.* 7, 9371–9389.
- Paterson, W.S.B., 2016. *The Physics of Glaciers*. Elsevier.
- RGI Consortium, 2017. *Randolph Glacier Inventory – A Dataset of Global Glacier Outlines: Version 6.0. Technical Report, Global Land Ice Measurements from Space. Digital Media, Colorado, USA.*
- Rignot, E., Buscarlet, G., Csatho, B., Gogineni, S., Krabill, W., Schmeltz, M., 2000. Mass balance of the northeast sector of the Greenland ice sheet: a remote-sensing perspective. *J. Glaciol.* 46, 265–273.
- Rignot, E., Mouginot, J., 2012. Ice flow in Greenland for the international polar year 2008–2009. *Geophys. Res. Lett.* 39.
- Rizzoli, P., Martone, M., Gonzalez, C., Wecklich, C., Borla Tridon, D., Bräutigam, B., Bachmann, M., Schulze, D., Fritz, T., Huber, M., et al., 2017a. Generation and performance assessment of the global TanDEM-X digital elevation model. *ISPRS J. Photogr. Remote Sens.* 132, 119–139.
- Rizzoli, P., Martone, M., Rott, H., Moreira, A., 2017b. Characterization of snow facies on the Greenland Ice Sheet observed by TanDEM-X interferometric SAR data. *Remote Sens.* 9, 315.
- Sasgen, I., van den Broeke, M., Bamber, J.L., Rignot, E., Sørensen, L.S., Wouters, B., Martinec, Z., Velicogna, I., Simonsen, S.B., 2012. Timing and origin of recent regional ice-mass loss in Greenland. *Earth Planet. Sci. Lett.* 333–334, 293–303. <https://doi.org/10.1016/j.epsl.2012.03.033>.
- Schröder, L., Horwath, M., Dietrich, R., Helm, V., van den Broeke, M.R., Ligtenberg, S.R.M., 2019. Four decades of Antarctic surface elevation changes from multi-mission satellite altimetry. *Cryosphere* 13, 427–449. <https://doi.org/10.5194/tc-13-427-2019>. URL: <https://www.the-cryosphere.net/13/427/2019/>.
- Schröder, L., Richter, A., Fedorov, D.V., Eberlein, L., Brovkov, E.V., Popov, S.V., Knöfel, C., Horwath, M., Dietrich, R., Matveev, A.Y., et al., 2017. Validation of satellite altimetry by kinematic GNSS in central East Antarctica. *Cryosphere* 11, 1111–1130.
- Shean, D.E., Alexandrov, O., Moratto, Z.M., Smith, B.E., Joughin, I.R., Porter, C., Morin, P., 2016. An automated, open-source pipeline for mass production of digital elevation models (DEMs) from very-high-resolution commercial stereo satellite imagery. *ISPRS J. Photogrammetry Remote Sens.* 116, 101–117.
- Shepherd, A., Ivins, E., Rignot, E., Smith, B., Van Den Broeke, M., Velicogna, I., Whitehouse, P., Briggs, K., Joughin, I., Krinner, G., et al., 2018. Mass balance of the Antarctic ice sheet from 1992 to 2017. *Nature* 556, 219–222.
- Shepherd, A., Ivins, E.R., Geruo, A., Barletta, V.R., Bentley, M.J., Bettadpur, S., Briggs, K.H., Bromwich, D.H., Forsberg, R., Galin, N., et al., 2012. A reconciled estimate of ice-sheet mass balance. *Science* 338, 1183–1189.
- Sonka, M., Hlavac, V., Boyle, R., 2014. *Image processing, analysis, and machine vision*, 4th edition. Cengage Learning ISBN 13: 9781133593607.
- Straehle, C.N., Koethe, U., Knott, G., Briggman, K., Denk, W., Hamprecht, F.A., 2012. Seeded watershed cut uncertainty estimators for guided interactive segmentation. In: *Computer Vision and Pattern Recognition (CVPR)*, 2012 IEEE Conference on, IEEE, pp. 765–772.
- Van der Veen, C.J., 2013. *Fundamentals of Glacier Dynamics*. CRC Press.
- Vincent, L., Soille, P., 1991. Watersheds in digital spaces: an efficient algorithm based on immersion simulations. *IEEE Trans. Pattern Anal. Mach. Intell.* 13, 583–598.
- Wessel, B., Bertram, A., Gruber, A., Bemm, S., Dech, S., 2016. A new high-resolution elevation model of Greenland derived from TanDEM-X. *ISPRS Ann. Photogr. Remote Sens. Spatial Inf. Sci.* 3, 9–16.
- Zink, M., Bachmann, M., Brautigam, B., Fritz, T., Hajnsek, I., Moreira, A., Wessel, B., Krieger, G., 2014. TanDEM-X: the new global DEM takes shape. *IEEE Geosci. Remote Sens. Mag.* 2, 8–23.
- Zwally, H.J., Giovinetto, M.B., Beckley, M.A., Saba, J.L., 2012. *Antarctic and Greenland drainage systems, GSFC cryospheric sciences laboratory*. Available at: http://icesat4.gsfc.nasa.gov/cryo_data/ant_grn_drainage_systems.php.